Superior synergy of g-C$_3$N$_4$/Cd compounds and Al-MOF-derived nanoporous carbon for photocatalytic hydrogen evolution

Malgorzata Aleksandrzak*, Daria Baranowska, Tomasz Kedzierski, Krzysztof Sielicki, Shuai Zhang, Marcin Biegun, Ewa Mijowska

West Pomeranian University of Technology, Faculty of Chemical Technology and Engineering, Department of Physicochemistry of Nanomaterials, Piastow Ave. 42, 71-065 Szczecin, Poland

ARTICLE INFO

ABSTRACT

Graphitic carbon nitride (gCN) exhibits outstanding photocatalytic performances toward H$_2$ evolution. However, it can be further improved by overcoming its disadvantages such fast recombination of pohotogenerated electron-hole pairs. Here, we propose an efficient photocatalysts based on three components: (i) gCN modified with (ii) cadmium compounds (CdX: Cd(OH)$_2$, CdS, CdO) and (iii) nanoporous carbon flakes (NPC) derived from Al-metal organic framework. The fabrication method was focused on finding the optimal hybrid composition dispaling the most powerful performance. Three main aspects were revealed: (i) band gap of gCN narrowing from 2.70 eV to 2.32 eV, (ii) reduction of overpotential for H$_2$ evolution, as conduction band minimum (CBM) moved from -1.07 V vs. NHE to -0.63 V vs. NHE and (iii) enhanced charge separation, since CdX and NPC acted as electron acceptors. These factors had an effect on ~60-fold enhancement of the photocatalytic efficiency. The mechanism of the photocatalytic process was discussed.

1. Introduction

The energy storage and environmental issues have gained enormous research focus in recent years. The semiconductor-based photocatalysis has occurred with prodigious superiority because it is considered as an economic, renewable, clean and safe technology [1,2]. It requires only the infinite solar light, as a driving force, and a suitable semiconductor, as a photocatalyst, to conduct catalytic reactions for a variety of applications e.g. in hydrogen production from water splitting [3,4], CO$_2$ reduction into hydrocarbon fuels [5], decomposition and mineralization of organic pollutants [6], selective organic synthesis [7] and even disinfection of bacteria [8]. Many semiconductors have been identified as potential photocatalysts under ultra-violet or visible light, such as TiO$_2$ [9,10], ZnO [11,12], SnO$_2$ [13,14], Fe$_2$O$_3$ [15,16], BiVO$_4$ [17,18], Cu$_2$O [19,20] and CdS [21,22]. Among them, graphitic carbon nitride has attracted great attention in the past several years because of its prominent catalytic, photocatalytic and photoelectrocatalytic properties [23–27]. This cheap, easily available, metal-free organic semiconductor demonstrates high performance in many energy-related fields. In general, the photocatalytic activity of semiconducting materials depends on their surface area, light absorption and efficiency of charge separation [27]. Therefore, the modification of graphitic carbon

nitride (g-C$_3$N$_4$) has been studied intensively. One of a semiconductor, that has been used as a co-catalyst for graphitic carbon nitride is cadmium sulfide [28,29]. CdS, a well-known visible-light-sensitive material [30], has been widely studied for the conversion of solar into chemical energy. However, the low separation efficiency of photogenerated electrons and holes and the fact that it is easily corroded [31,32] are not favorable for the wide applications of CdS in environmental remediation and solar conversion. Hence, recent attempts to improve photocatalytic performance of CdS focus on structure design or surface modification [33–38]. Q. Li et al. [39] reported modification of CdS rods with Cd(OH)$_2$ nanoparticles and evidenced that cadmium hydroxide significantly improved the photoactivity in hydrogen evolution reaction. It was mainly attributed to the presence of Cd^0 as an electron transport intermediary, which was produced by in-situ photoreduction of Cd(OH)$_2$ interfacial layer between CdS and Pt [39]. S. Meng et al. fabricated zero-dimensional NiS$_x$ nanosheets as a co-catalyst on the surface of 1-dimensional CdS nanorods to enhance the photocatalytic hydrogen evolution [40].

Another group of materials, that can be used for enhancement of photocatalytic performance of graphitic carbon nitride or cadmium sulfide, is nanostructured carbon, such as carbon nanotubes (CNTs), fullerenes, graphene, carbon quantum dots and other [41]. X. H. Jiang

et al. [42] coupled graphitic carbon nitride with carbon quantum dots (CQDs) and CdS quantum dots and showed that CQDs emitted up-converted light, enhancing light harvesting by CdS and g-C_3N_4, and behaved as electron acceptor, enhancing charge separation and efficiency of photocatalysis. R. C. Pawar et al. modified gCN with cadmium sulfide and reduced graphene oxide and admitted beneficial properties of carbon nanostructure [43].

To the best of our knowledge, there is no report on utilization of nanostructured carbon derived from metal organic framework, as a co-catalyst for photocatalysis. Therefore, we investigated a co-modification of graphitic carbon nitride with cadmium based compounds and nanoporous carbon (NPC) derived from Al-MOF. Cadmium compounds and nanoporous carbon significantly enhanced photocatalytic H_2 production in comparison to pristine gCN. The morphology, chemical structure, optical, photophysical and electronic properties of the resulting carbon nitrides are fully characterized by microscopic and spectroscopic techniques. The photocatalytic activity was investigated by measuring the release of H_2 during water reduction in the presence of the prepared catalysts.

2. Experimental

2.1. Synthesis of graphitic carbon nitride

Graphitic carbon nitride was prepared via calcination of urea in a muffle furnace at 550 °C for 4 h in air. The temperature was achieved with a heating rate of 2 °C/min. After the reaction, the furnace was cooled down to room temperature in air atmosphere.

2.2. Synthesis of cadmium compounds (CdX)

Firstly, 100 mL of 1 M $NH_3 \cdot H_2O$ water based solution was prepared, followed by addition of 5 mM CH_4N_2S. After few minutes, 1 mM $CdSO_4$ was added and the temperature was set at 60 °C. The reaction mixture was magnetically stirred for 10 min. Afterwards, the solid material was filtered and dried in air at 100 °C.

2.3. Synthesis of nanoporous carbon

Nanoporous carbon (NPC) was synthesized according to our well established method [44] and it was composed of three main steps: (i) synthesis of Al-MOF, (ii) carbonization of Al-MOF and (iii) removal of Al with HCl solution. Briefly, 1.875 g $Al(NO_3)_3 \cdot 9H_2O$ and 0.81 g 1,4-Benzenedicarboxylic acid (BDC) were dissolved in 40 mL *N,N*-Di-methylmethanamide (DMF), then the mixture was 30 min ultra-sonicated to make a homogeneous solution. Subsequently, the solution was heated to 150 °C for 48 h under stirring and reflux. After cooling to room temperature, the solution was centrifuged at 8000 rpm, and white crystals were collected. The as-prepared material was washed 3 times by DMF to remove the impurities. Then, the material was dried at 60 °C under vacuum, after exchanging of DMF with dichloromethane for 24 h. The carbonization of Al-MOF proceeded as follows: 2 g of the Al-based metal-organic was put into a quartz boat, and heated to 750 °C for 3 h in Ar atmosphere. The sample, in the form of black powder, was collected after the furnace was cooled down to room temperature. Finally, aluminum was removed from carbonized Al-MOF in 10 mL 17% HCl and refluxing at 120 °C for 4 h. The sample was filtered via 0.2 μm porous film, and washed 5 times with DI water. Then the final product was dried at 75 °C in vacuum.

2.4. Synthesis of CdX-gCN nanocomposite

Graphitic carbon nitride was dispersed in water (0.1 mg/mL) and the mixture was sonicated for 1 h. Next, 1 M $NH_3 \cdot H_2O$ and 2.5 mM CH_4N_2S were added and it was magnetically stirred for few minutes until CH_4N_2S was dissolved. Then, 0.5 mM $CdSO_4$ was introduced and

the reaction mixture was magnetically stirred for 10 min. The final product was achieved by filtration and drying in air at 100 °C. $Cd(OH)_2$/CdS-gCN nanocomposites were obtained with different CdX amount (20 wt%, 40 wt% and 60 wt% for CdX-gCN, CdX40-gCN and CdX60-gCN, respectively).

2.5. Synthesis of CdX-gCN-NPC nanocomposite

NPC was dispersed in water and sonicated for 12 h. Next, the appropriate amount of $Cd(OH)_2$/CdS40-gCN was added and the suspension was sonicated and stirred overnight. $Cd(OH)_2$/CdS40-gCN-CMOF nanocomposite with different NPC concentration (2 wt%, 5 wt% and 10 wt% for CdX-gCN-NPC2, CdX40-gCN-NPC5 and CdX40-gCN-NPC10, respectively) was finally obtained by drying in air at 100 °C.

2.6. Characterization

The morphology of the samples was examined via transmission electron microscopy (TEM, Tecnai F30). X-ray diffraction (XRD) study was carried out using X'Pert Philips Brunauer-Emmett-Teller (BET) specific surface area and pore volume were measured by nitrogen sorption in the temperature of liquid nitrogen using a Micromeritics ASAP 2460. The pore size distribution of each sample was calculated using non-local density functional theory (NLDFT), from the desorption branch of the isotherms. Diffractometer with Cu lamp to investigate the crystal structure of the samples. FTIR absorption spectra were recorded on Nicolet 6700 FT-IR Spectrometer. The X-ray photoelectron spectroscopy (XPS) analysis was performed in the presence of Mg K_a (hν = 1253.6 eV) radiation. A Prevac (Poland) electron spectrometer for chemical analysis system equipped with Scienta (Sweden) SES 2002 electron energy analyzer operating at constant transmission energy (E_p = 50 eV) was used. The analysis chamber was evacuated to the pressure below $1 \cdot 10^{-9}$ mbar. A powdered sample of the material was placed on a stainless steel sample holder. The room temperature photo-luminescence (PL) spectroscopy measurements at 280 nm excitation were performed using fluorescence spectrophotometer F 7000 (Hitachi). The optical properties of the materials were investigated by means of the diffuse reflectance spectroscopy (DRS), using a Jasco (Japan) spectrometer. Band gap energy values were calculated from equation $E_g = \frac{hc}{\lambda}$. The electrochemical tests were performed by means of BioLogic VMP-3 potentiostat station in a three-electrode cell. The temperature of the set was thermostated by a Hubner KISS 6 (Germany) temperature control bath at 25 °C ± 0.05 °C. The reference electrode was a saturated calomel electrode Hg|Hg_2Cl_2, KCl(sat.) (SCE), a counter electrode, platinum wire (Surface area ~5 cm^2). The working electrode (WE) was a 5 mm diameter glassy carbon disk in PEEK polymer case (ALS Co., Ltd, Japan). The surface of WE was prepared/activated by polishing with 0.05 μm alumina slurry and washed with ultrapure water. The catalyst dispersion with 2 mg/mL mass loading in iso-propanol was drop-casted and left to dry for 12 h in air. WE surface preparation quality was inspected by optic stereomicroscope (Zeiss Germany). The measurements were performed in water solution of redox salts $K_3[Fe(CN)_6]$/$K_4[Fe(CN)_6]$, 2.5 mM/2.5 mM with 0.5 M so-dium sulfate as base electrolyte. Mott-Schottky test, performed by an Electrochemical Impedance Spectroscopy, was set up with frequency range of 20 kHz to 0.1 Hz with 5 mV AC signal amplitude, 11 points per decade, at potential from 0.8 V to -0.5 V vs SCE with 26 potential steps (-50 mV shift, 15 min equilibration time). Linear Sweep Potentiometry and Photocurrent response measurements were conducted by Autolab PGSTAT302 N potentiostat in a 3-electrode test cell with a platinum wire as Counter electrode and Saturated Calomel Electrode as reference. Examined material was drop-casted and dried from 0.2% ethanol/nafion solution at FTO glass slide (Sigma Aldrich) as a working electrode. Glassy working electrode was fixed inside the test cell as a light stream target. 0.5 M sodium sulfate was used as the electrolyte.

LSV test was performed from 0.15 V to 1.4 V vs SCE with 50 mV/s scan rate. Photocurrent (Chronoamperometry) test was measured at 0.5 V vs SCE.

2.7. Photocatalytic hydrogen evolution

Photocatalytic hydrogen evolution reactions were conducted in an outer irradiation-type reactor (Pyrex glass) connected to argon. 10 mg of a photocatalyst was dispersed in 20 mL of water and sonicated for 1 h. After that, 2 mL of lactic acid was poured and the reactor was purged with argon to remove air, followed by irradiation with 150 W Xe lamp. An air mass filter (A.M. 1.5 G) was utilized to achieve the simulated solar light. The photocatalytic H_2 evolution rate was analyzed using Young Lin 6500 gas chromatograph (GC, Micro TCD detector, HayeSep A – Valco PLOT Capillary Columns and Ar as a carrier). Five cycles of experiments were carried out to investigate the stability of the photocatalyst. Each test was carried out for 4 h under the irradiation. After each test, the gaseous products were evacuated, and the reactor was purged with argon.

The apparent quantum efficiency at $\lambda_0 = 426$ nm (+/- 20 nm) was calculated for CdX40-gCN-NPC5 photocatalyst. The average intensity of irradiation was determined to be 2.6 mW·cm^{-2} and the irradiation area was 4.9 cm^2. The number of incident photons (N) in 4 h is $3.93 \cdot 10^{-20}$ as calculated by the following Eq. (1):

$$N = \frac{E\lambda}{hc} \tag{1}$$

The amount of H_2 molecules generated in 4 h was 4.66 µmol. The quantum efficiency is estimated basing on Eq. (2):

$$AQE = \frac{2x\ the\ number\ of\ evolved\ H_2\ molecules}{the\ number\ of\ incident\ photons} \tag{2}$$

3. Results and discussion

3.1. Morphology and chemical structure

The morphology of the prepared materials was characterized with transmission electron microscopy and images are presented in Fig. 1. Graphitic carbon nitride synthesized from urea is composed of nanosheets with tendency to fold and to aggregate. High resolution TEM image (Fig. 1b) revealed that gCN is characterized by pores with diameters ranging from 5 to 10 nm. These nanopores are perfect places for deposition of guest nanoparticles. Nitrogen adsorption-desorption isotherms (Fig. S1) of gCN demonstrated relatively high BET specific surface of 139.8 m^2/g and the pore volume of 0.131 cm^3/g. TEM images of nanoporous carbon are presented in Fig.1c–d. The carbonization, followed by HCl treatment of Al-MOF, influenced formation of individual carbon nanoparticles with diameters of 12–22 nm. Basing on our previous study [44] NPC is characterized by BET surface area of 809 m^2/g and average pore diameter of 1.51 nm with total pore volume of 3.087 cm^3/g (Fig. S1). Further TEM analysis showed that cadmium compounds formed irregular shapes with average diameter of 4 nm (nanoparticles size distribution in the inset of Fig. 1e. The synthesis of CdX in the presence of graphitic carbon nitride resulted in homogeneous distribution of the nanoparticles on the surface of gCN. Moreover, increase in the CdX nanoparticles diameters to the average value of 8 nm was observed. Simultaneously, BET surface area and pore volume decreased to 76.81 m^2/g and 0.085 cm^3/g, respectively. NPC nanoparticles were hard to observe when functionalized with CdX-gCN. However, it was noticed that after NPC addition, the BET surface area of CdX-gCN-NPC increased to 91.7 m^2/g and the pore volume decreased to 0.044 cm^3/g.

Atomic force microscopy is a useful technique utilized for determination of topography and thickness of two-dimensional nanomaterials. Fig. 2 presents AFM images and height profiles of graphitic
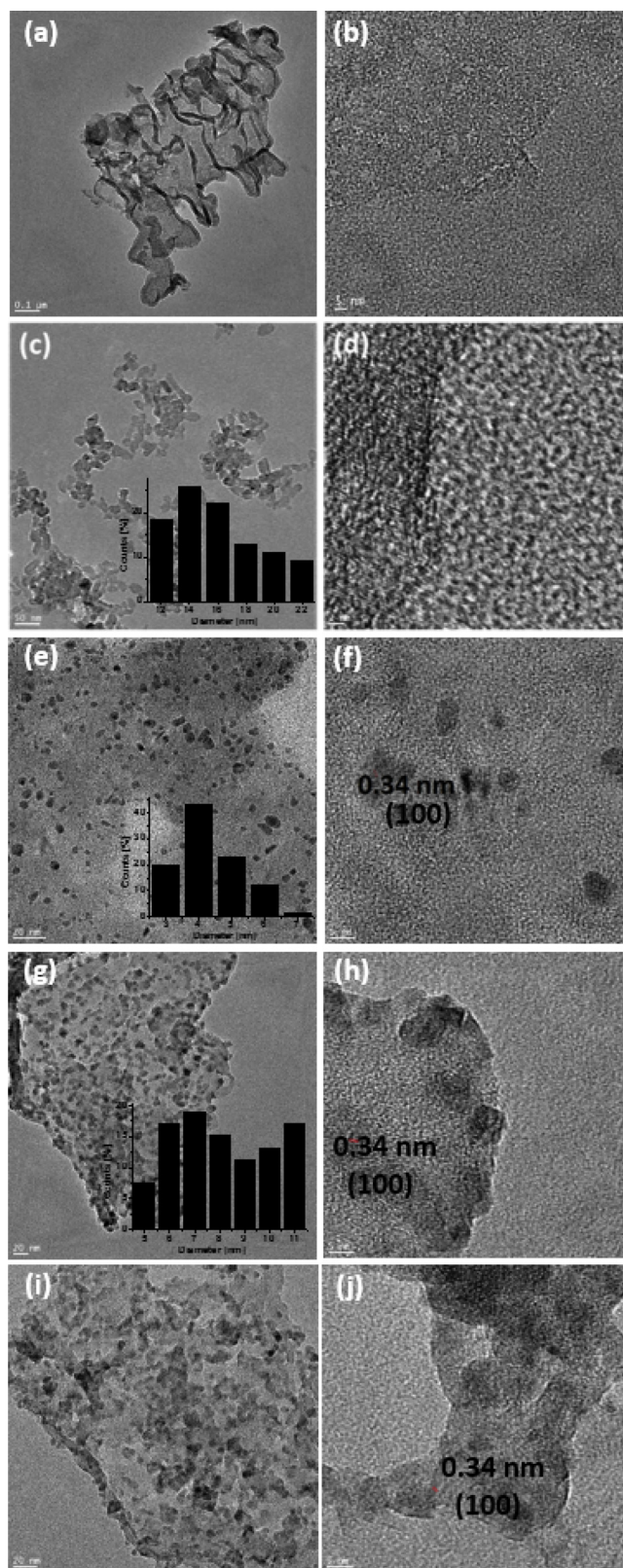

Fig. 1. TEM images of gCN (a–b), CdX (c–d), NPC (e–f), CdX-gCN (g–h) and CdX-gCN-NPC5 (i–j). The insets present nanoparticles size distribution.

carbon nitride and nanoporous carbon flakes. The analysis revealed that gCN is composed of nanosheets with thickness of ~3.5 nm, while the thickness of NPC nanoflakes is in the range of 0.5–7.4 nm. It means that the carbon nitride is composed of approximately 11 layers, while NPC is
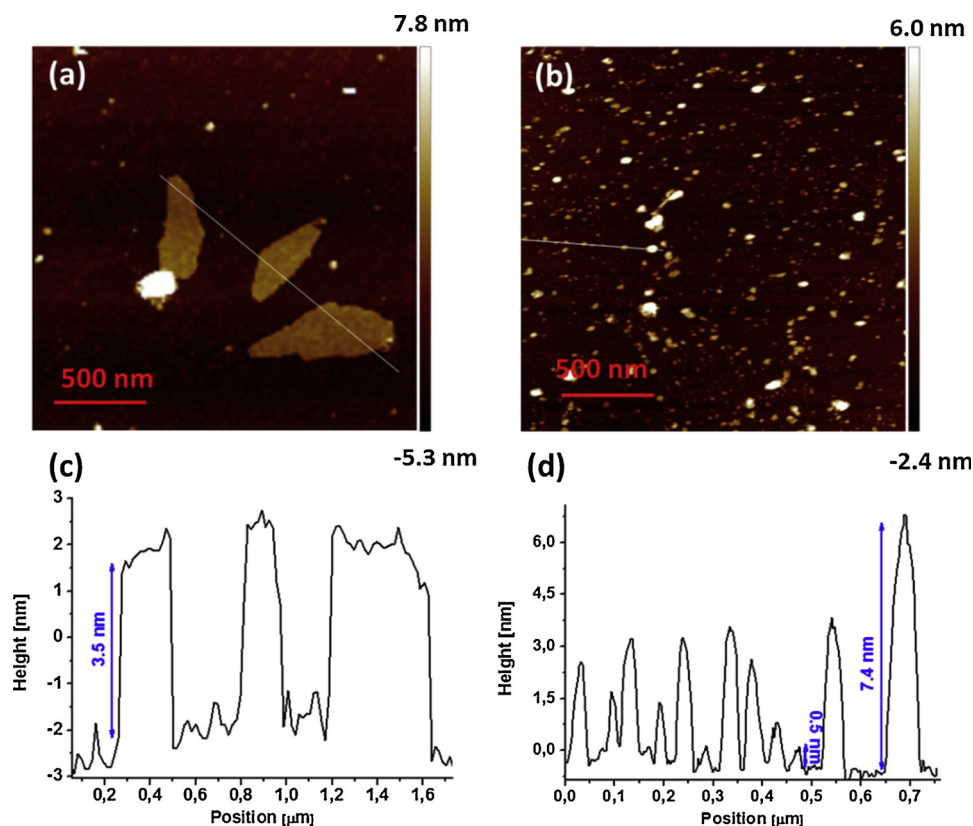
Fig. 2. AFM images and height profiles of gCN (a, c) and NPC (b, d).

a mixture of single–, bi– and few–layered carbon flakes.

Fourier Transform Infrared (FTIR) Spectroscopy and X-ray Diffraction (XRD) were used to determine the chemical structure and local order of the carbon nitrides. FTIR absorption analysis was recorded in the spectral range of 400–4000 cm^{-1} to examine the surface of the prepared gCN, CdX CdX-gCN, NPC and CdX40-gCN-NPC5, and it is shown in Fig. 3a. The peak at 809 cm^{-1} in the spectra of gCN, CdX40-gCN and CdX40-gCN-NPC5 belongs to the s-triazine ring models, which corresponds to the condensed CN heterocycles. The bands at 1200–1600 cm^{-1} are characteristic for aromatic C–N heterocycles [45–49]. To be more specific, the absorption bands near 1242, 1319 and 1409 cm^{-1} are attributed to aromatic C–N stretching, while 1572 and 1637 cm^{-1} correspond to C=N stretching. The broad band at 3000–3500 cm^{-1} corresponds to uncondensed terminal amino groups (-NH$_2$ or = NH groups) [50,51]. Clearly, the FTIR spectra of Cd(OH)$_2$/CdS40-gCN-NPC5 and Cd(OH)$_2$/CdS40-gCN are similar to that of gCN, indicating that the nanocomposites keep the same chemical structure as their parent gCN. The band at around 3600 cm^{-1}, observed in the spectra of gCN and CdX40-gCN, is assigned to the OH-stretching vibrations of hydroxyl group [52]. In the spectrum of CdX, the broad bands centered at 1635 and 3462 cm^{-1} are related to the hydroxyl groups of Cd(OH)$_2$. Furthermore, the characteristic bands at 1129 and 1385 cm^{-1} correspond to the Cd—S bond [53]. The absorption spectra of CdX40-gCN-NPC5 and CdX40-gCN are characterized by the bands characteristic for both gCN and CdX, confirming the hybrid composition. For NPC, the bands at 1560 and 1705 cm^{-1} are related to C=C stretching vibrations of aromatic rings. The bands at 2863 – 2955 cm^{-1} arise from C–H groups.

The crystal structure and phases purity of the as-synthesized gCN, CdX, CdX40-gCN, NPC and CdX40-gCN-NPC5 were monitored using the X-ray diffraction (XRD). Fig. 3b shows the XRD diffraction patterns of the samples. As shown in Fig. 2b, in the XRD pattern of gCN, CdX40-gCN and CdX40-gCN-NPC5 the peak at 27.7° is attributed to the (002) reflection of a graphitic-like aromatic structure, whereas the peak at

13.1° is attributed to the (100) [54] and corresponds to the in-plane repeating motifs of the continuous heptazine network [45–49]. XRD peaks of CdX can be prominently indexed at 2θ values of 18.8°, 29.5°, 35.2°, 38.1°, 49.7°, 52.4°, 59.0°, 61.2°, 64.7°, 66.8°, 74.6°, 84.6° and 87.8°. They are related to the monoclinic crystalline structure of Cd (OH)$_2$ [50]. The diffraction peaks correspond to (001), (100), (101), (002), (102), (110), (003), (200), (201), (112) and (202) planes of Cd (OH)$_2$ crystal system [55,56], respectively. Those peaks are also observed in the XRD pattern of Cd(OH)$_2$ (JCPDF File No. 01-073-0969). The peaks observed at 2θ values of 26,6°, 44,5°, 51,6° and 54,1° match with the (002), (110), (200) and (004) [57] crystalline planes of the hexagonal structure of CdS in the reference patterns of JCPDF File No. 00-001-0647. The prepared composites are considered to possess a highly crystalline nature as the diffraction peaks are relatively sharp. In the diffraction pattern of CdX40-gCN, both gCN and CdX were detected, indicating that synthesized composite materials contain both of the constituent phases. However, when CdX is added, the intensity of the CdX peaks increased, whereas the gCN peaks intensity decreased. It can be due to the gradual covering of the gCN surface by CdX. XRD peaks of NPC at 22.4° is attributed to (002) reflection of carbon structure and 44.2° is attributed to (101) and corresponds to the axis of graphitic structure [58–63]. Therefore, the presence of these peaks emphasizes the successful formation of CdX40-gCN-NPC composite.

X-ray photoelectron spectroscopy was utilized to analyze the chemical composition and state of the surface of the following samples: gCN, CdX and CdX-gCN. The XPS spectra of C 1s and N 1s regions for gCN and Cd 3d, S 2p and O 1s regions for CdX are presented in Fig. S2, while atomic concentration of the respective elements is presented in Fig. 3d. The surface of gCN contains carbon and nitrogen atoms in atomic ratio of 0.66, relatively close to the theoretical value based on gC$_3$N$_4$ stoichiometric formula (namely 0.75). The surface of CdX is composed of cadmium, oxygen, sulfur and carbon, with atomic percentage of 36, 35, 10 and 19 at.%, respectively. It suggest that CdX is composed of Cd(OH)$_2$, CdS, CdO and carbon. Basing on the atomic
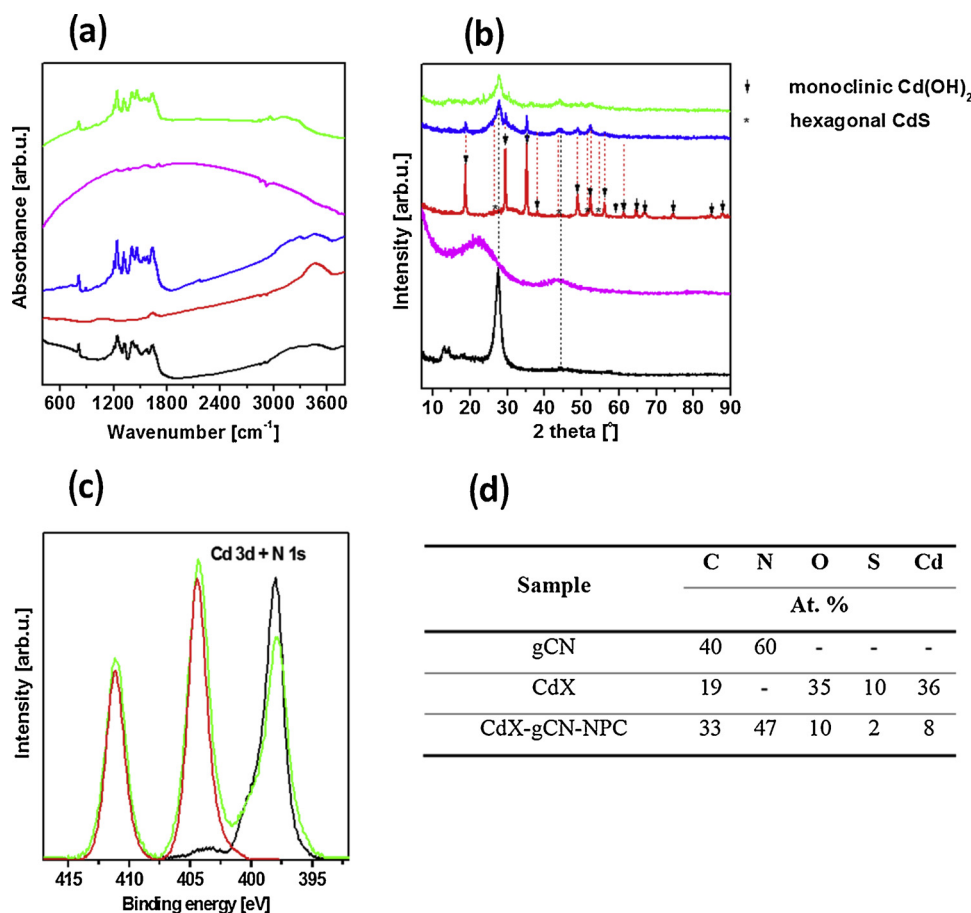
Fig. 3. (a) FTIR spectra and (b) XRD patterns, (c) XPS spectra in Cd 3d and N 1s regions. (d) The atomic concentration of carbon, nitrogen, oxygen, sulfur and cadmium on the surface of gCN, CdX and CdX-gCN-NPC calculated on the basis of XPS signals. Black line corresponds to gCN, red line – CdX, blue line – CdX-gCN, magenta line – NPC and green line – CdX-gCN-NPC.

Sample	C	N	O	S	Cd
	At. %				
gCN	40	60	-	-	-
CdX	19	-	35	10	36
CdX-gCN-NPC	33	47	10	2	8

concentration, mass concentrations of Cd(OH)$_2$, CdS, CdO and carbon were calculated to be 29 wt.%, 29 wt.%, 38 wt.% and 4 wt.%, respectively.

The analysis of chemical states of the considered samples is based on the high-resolution XPS spectra. The combined region of XPS Cd 3d and N 1s peaks is shown in Fig. 3c. The maximum of XPS N 1s peak observed for gCN sample is located at 398.2 eV. There is also a notable shoulder on the high-energy side of that peak - at approximately 400 eV. These two regions are usually reported for the different carbon nitride samples [64,65]. The N 1s peaks in the range between 398 eV and 399 eV are generally assigned to nitrogen atoms bonded to sp^3-hybridized carbon atoms. The chemical shift toward higher energy of 400.0 eV is attributed to the contribution of nitrogen atoms bonding to sp^2-hybridized carbon [66,67].

The XPS spectrum of Cd 3d region acquired for CdX sample is composed of two distinctive peaks. They are assigned to Cd 3d$_{5/2}$ and Cd 3d$_{3/2}$ lines and are located at 404.5 eV and 414.2 eV, respectively. These positions correspond to the presence of Cd^{2+} ions [68,69].

The XPS spectrum of Cd 3d and N1 s regions in the composite of CdX-gCN sample is in general a simple superposition of the respective lines observed for CdX and gCN samples separately. There is no chemical shift observed for cadmium and nitrogen. It can be concluded that the preparation of the composite does not induce any changes in the chemical states of the considered compounds.

3.2. Optical and band structure properties

Optical properties of the materials were characterized with assistance of DRS spectroscopy and the results are presented in Fig. 4a. The absorption edge of graphitic carbon nitride is positioned at approximately 459 nm, which corresponds to the optical band gap of 2.7 eV.

This value is fully consistent with the literature [64]. In comparison to gCN, CdX is characterized by stronger absorption of the visible light with an absorption edge at 611 nm corresponding to E$_g$ = 2.03 eV. Basing on the state of the art, Cd(OH)$_2$, CdS and CdO are characterized by band gap of 3.35, 3.12 – 2.47 (depending on nanoparticles size) and 2.18 eV, respectively [70–72]. The enhanced absorption of visible light and red shift of absorption edge in our sample might be attributed to the presence of carbon (4 wt.%). Addition of 40 wt.% of CdX to gCN resulted in the enhancement of the absorption over the whole range of the investigated wavelengths and red-shift of the absorption edge to 549 nm, which is related to the band gap energy of 2.26 eV. DRS spectrum of nanoporous carbon is characterized by the strong absorption of the visible light with no absorption edge. Addition of this material to the nanocomposite (CdX-gCN- NPC) resulted in blue-shift of the absorption edge in respect to the nanocomposite without NPC (CdX-gCN). The absorption edge is positioned at 535 nm what corresponds to the band gap energy of 2.32 eV.

Except of a suitable band gap, photocatalytic water splitting is possible when valence and conduction band levels are in the positions, that enable oxidation and reduction of water, leading to oxygen and hydrogen evolution, respectively. In order to estimate a position of a conduction band (CB), a flat-band potential, which is close to the CB edge [73,74], can be determined from the Mott–Schottky Eq. (3):

$$\frac{1}{C^2} = \frac{2}{\varepsilon\varepsilon_0 A^2 e N_D}(V - V_{fb} - \frac{k_B T}{e})$$

$$(3)$$

where, C is the capacitance of the space charge layer, e is the charge of electron, ε$_o$ is free space permittivity, ε is dielectric constant, V is applied potential, V$_{fb}$ is flat–band potential, N$_D$ is donor density or donor concentration, k is Boltzmann constant and T is Kelvin temperature. Therefore, a plot of 1/C^2 against V should yield a straight line from which V$_{fb}$ can be determined from the intercept on the V axis [75].
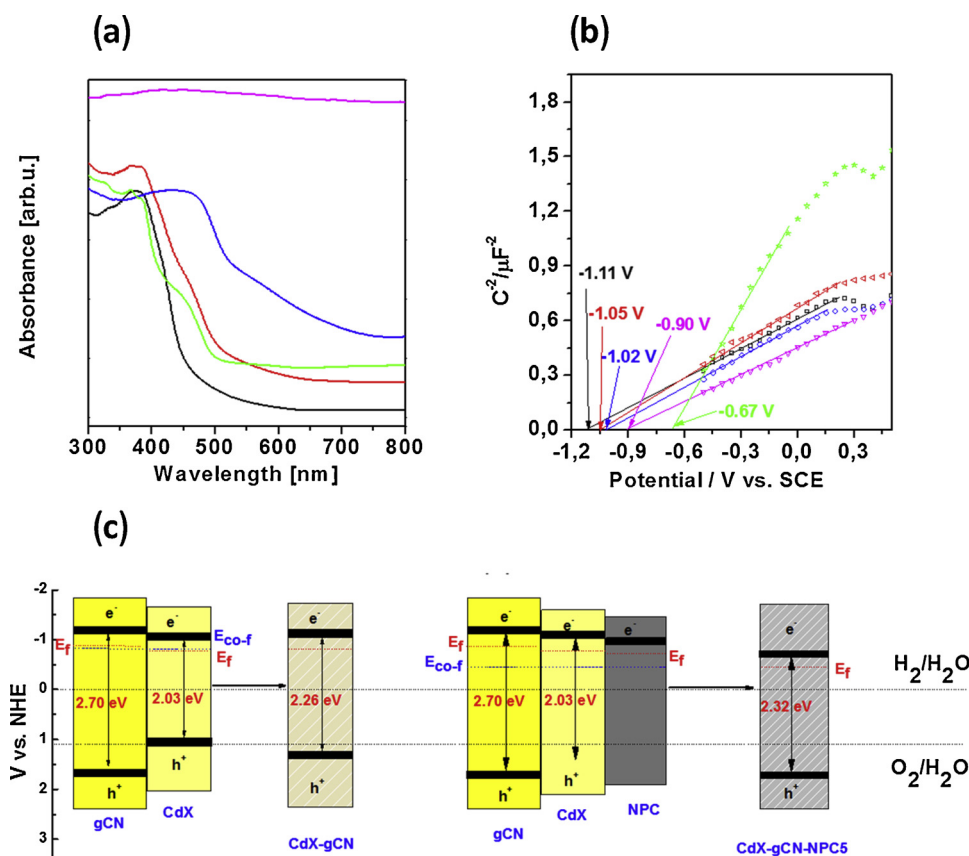
Fig. 4. (a) DRS spectra, (b) Mott- Schottky plots with determined flat band potentials, (c) Band structure diagram of gCN (black line), CdX (blue line), CdX-gCN (red line), NPC (magenta line) and CdX-gCN- NPC (green line).

Mott-Schottky plots of selected photocatalysts are presented in Fig. 4b. The samples show positive slope indicating n-type semiconductor [73]. Flat band potential of gCN, CdX, CdX-gCN, NPC and CdX40-gCN-NPC5 was found to be at -1.11, -1.02, -1.05, -0.90 and -0.67 V vs. SCE, respectively. Since conduction band minimum (CBM) of an n-type semiconductor is generally more negative of about -0.1 or -0.2 V than its flat band potential, the CBM of the materials are the following: -1.07, -0.98, -1.01, -0.86 and -0.63 V vs. NHE, for gCN, CdX, CdX-gCN, NPC and CdX-gCN-NPC5, respectively. The offset between Fermi level (E_f) and CBM was estimated according to the Eq. (4) [76]:

$$CBM - E_f = \frac{kT}{e} \cdot ln \frac{N_C}{N_D} \tag{4}$$

where k, T and N_C are Boltzmann constant, temperature and the effective density states at the bottom of the conduction band, respectively.

The flat band potentials and Fermi levels determined with Mott-Schottky analysis combined with the bandgap energy, allow the calculation of the valence band (VB) edge and the representation of the band structure diagram, which is presented in Fig. 4c. The CBM of CdX-gCN is more negative than that of CdX. This is caused by the carbon nitride, which pulls the Fermi level toward negative energy, resulting in the formation of co-Fermi level (E_{co-f}) [77]. Owing to the different E_f of gCN and CdX, the electrons from conduction band of gCN will be transferred to the CB of CdX until the energy balance is achieved. Then, the E_{co-f} will be positioned between them. When nanoporous carbon was introduced to CdX-gCN, the CBM was shifted toward positive energy because E_f of NPC is more positive than that of gCN and cadmium compounds. The Fermi level of CdX-gCN will be pulled positively upon interaction with NPC, leading to the formation a new balance.

3.3. Photoluminescence and photoelectrochemical properties

Photoluminescence spectroscopy is a method used to compare the lifetime and trapping of photogenerated electron-hole pairs, what directly influence the photocatalytic response. Isopropanol dispersions of the samples with the same concentrations were excited with irradiation of 380 nm and the emission spectra in the wavelength range of 400–670 nm are presented in Fig. 5a. PL spectrum of bulk graphitic carbon nitride shows three emission centers located at 438 nm (2.82 eV), 460 nm (2.69 eV) and 498 nm (2.49 eV), which are attributed to the electronic transitions between δ* conduction band and lone pair (LP) valence band, π* conduction band – LP and π* – π, respectively [78]. PL spectra of $Cd(OH)_2$/CdS and NPC are characterized by low emission of the photoluminescence. The deposition of CdX nanoparticles on gCN did not affect PL quenching, significantly. It could be attributed to the band structure of the two components. According to the Mott-Schottky analysis, CdX-gCN represents I-type heterojunction, since both CB and VB edges of CdX are between CB and VB edges of gCN. Hence, photogenerated electrons and holes could be transferred from gCN to CdX, resulting in minor separation of charge carriers and slight diminishing of PL. However, different emission trend is observed in the spectrum of CdX-gCN (red line). More accurately, weakening of the first emission center is observed, showing that PL emission peak is dominated by π* – π transitions. Co-modification of the photocatalyst with nanoporous carbon resulted in strong quenching of PL (green line) indicating synergistic effect of CdX and NPC nanoparticles. NPC can be responsible for the acceptance of the photogenerated electrons transferred from conduction band of graphitic carbon nitride and CdX. This effect might have significant influence on the photocatalytic properties of the four-component photocatalyst.

The time-resolved emission decay spectra, shown in Fig. 5b, were further recorded to better understand the separation of the
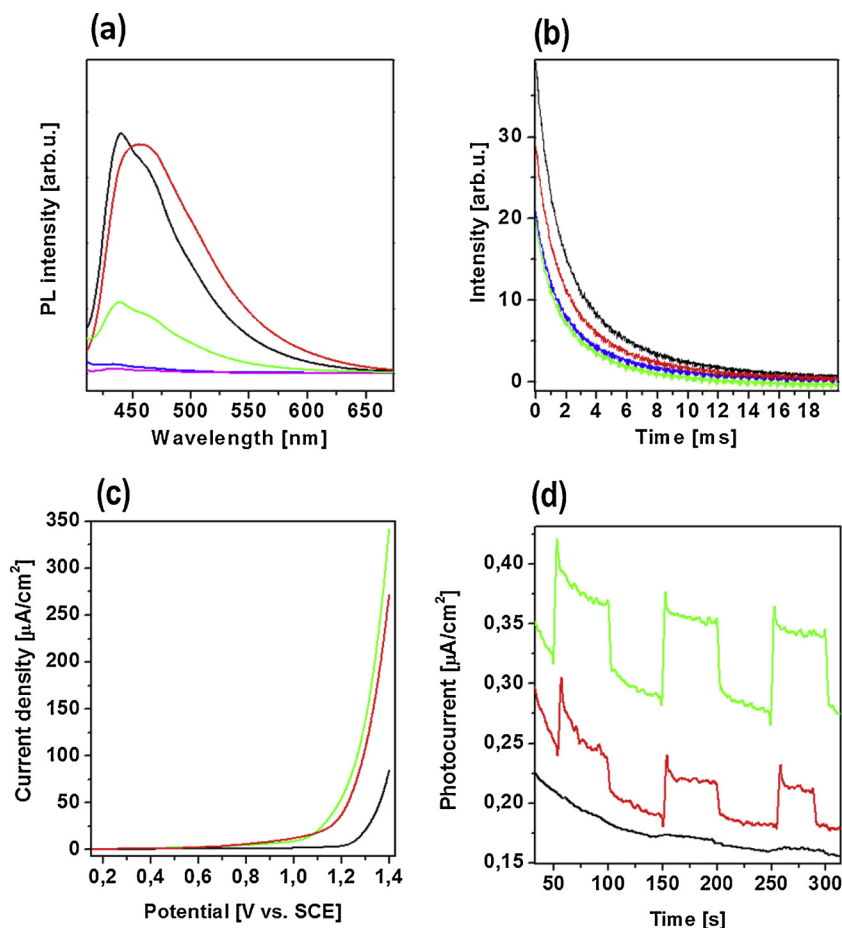
Fig. 5. (a) PL spectra, (b) time-resolved PL spectra, (c) LSV curves and (d) periodic on/off photocurrent response under 420–700 nm light. Black line corresponds to gCN, blue line – CdX, red line – CdX-gCN, magenta line – NPC and green line – CdX-gCN-NPC.

photoexcited charge carriers. The lifetimes were obtained by fitting the time-decay fluorescence curves using a single-exponential function. The PL lifetimes of gCN, CdX, CdX40-gCN and CdX40-gCN-NPC5 were found to be 2.270, 2.195, 2.242 and 2.018 ms, respectively. The PL lifetime decreased when gCN was combined with cadmium compounds and nanoporous carbon confirming improved separation of charge carriers [79].

For deeper understanding of the transport behavior of the photogenerated charge carriers, the LSV technique and transient photocurrent response were employed under irradiation of 420–700 nm (Fig. 5c,d). The intensity of the LSV response of graphitic carbon nitride was successfully enhanced when it was modified with cadmium compounds and nanoporous carbon. The same trend was observed in the results of the photocurrent response (Fig. 5d). It indicates the higher separation efficiency of the photogenerated charge carriers, which is in good agreement with the PL spectroscopy.

3.4. Photocatalytic hydrogen evolution

Hydrogen evolution in photocatalytic process performed on 20 mL of water with 10 mg of the photocatalyst, under simulated solar light, is presented in Fig. 7(a). Furthermore, the optimization of the photocatalyst composition was performed. As shown, the lowest amount of H_2 has been produced with use of pristine components (gCN, Cd(OH)$_2$/CdS) and two-component photocatalysts (gCN-NPC and CdX-NPC). The most efficient amount of cadmium compounds in the photocatalyst was established to be 40 wt.% and it evolved ~250 μmol/g of H_2 in 4 h. The lowest amount of CdX (20 wt.%) was nearly as effective as pristine graphitic carbon nitride, and the efficiency of the produced H_2 for the

sample with the highest amount of Cd compounds (60 wt.%) was about 150 μmol/g after 4 h. In similar way, the most efficient amount of nanoporous carbon was determined to be 5 wt.%. The efficiency of hydrogen evolution for CdX40-gCN-NPC5 was about 600 μmol/g. The addition of NPC significantly improved hydrogen production efficiency. Furthermore, the production rate of H_2 increased every hour in each composite. The most efficient nanocomposite was used for the determination of apparent quantum efficiency at 426 nm +/-20 nm. The amount of the evolved hydrogen was 466 μmol/g and AQE was found to be 1.42%.

In order to evaluate the photostability of the most efficient photocatalyst (CdX40-gCN-NPC5), five cycles of photocatalytic hydrogen evolution was performed (Fig. 6b). The experiment showed that the photocatalytic activity of the catalyst was stable for the entire five cycles, although, a slight decrease was observed. In the first cycle, the H_2 evolution rate was 148 μmol/g h, while after five cycles – 138 μmol/g h. Small decrease in the hydrogen evolution might be attributed to the consumption of lactic acid which was successively oxidized during the photocatalytic reaction. This effect was also observed by Gopannagari et al. [80]. The comparison of the valence and conduction band levels, the band gap energy and hydrogen evolution rate of the bare components and the optimized bi- and tri-component photocatalysts are presented in Table 1.

3.5. Mechanism of the enhanced photocatalytic hydrogen evolution over CdX-gCN-NPC photocatalyst

The above results clearly indicate that utilization of these three components as co-catalysts for photocatalytic hydrogen evolution is
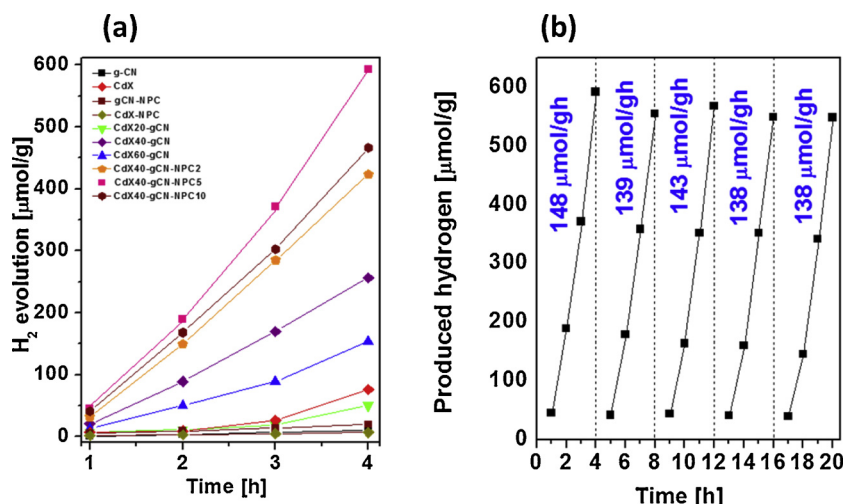
Fig. 6. (a) Hydrogen evolution catalyzed by gCN, CdX, gCN-NPC, CdX-NPC, CdX-gCN (20, 40 or 60 wt.% CdX), CdX40-gCN-NPC (2, 5 or 10 wt.% NPC). (b) Stability of CdX40-gCN-NPC5 during five cycles of prolonged photocatalytic hydrogen evolution reaction. Both graphs are based on the experiments conducted in 20 mL of water containing 0.01 g of the photocatalyst under simulated solar light (150-W Xe lamp using an A.M. 1.5 G filter).

reasonable. Moreover, the optimized composition of the hybrid has a significant impact on the efficiency of the process. The enhanced performance is related to several aspects. Firstly, it is the effect of band gap narrowing from 2.70 eV of gCN to 2.32 eV, when gCN was modified with CdX and nanoporous carbon. Band gap narrowing had an effect on the enhanced solar light harvesting. Secondly, addition of these two co-catalysts to graphitic carbon nitride resulted in pulling Fermi level and conduction band edge toward positive energy, hence, decreasing overpotential of proton reduction. Finally, since CBM of cadmium compounds and nanoporous carbon are more positive than the CBM of gCN, they could act as electron acceptors, what possibly improved the separation of charge carriers. These factors had a synergistic effect in the enhancement of the photocatalytic hydrogen evolution.

Basing on the above-mentioned analysis, we propose the mechanism of the photocatalytic hydrogen evolution reaction (Fig. 7). Under absorption of simulated solar light, graphitic carbon nitride and CdX were excited, leading to the transfer of electrons (e^-) to the conduction bands, and leaving holes (h^+) in the valence bands. The photoexcited electrons could migrate from gCN in two pathways: (i) to the surface reaction sites leading to photocatalytic reduction of protons and evolution of hydrogen, and (ii) to the surface of CdX. The second pathway was possible because CBM of gCN is more negative than the CBM of

Table 1

Characterization of conduction band (CB) and valence band (VB) levels, band gap energy (E_g) and hydrogen evolution rate (HER) of selected photocatalysts.

Photocatalyst	CB [V vs. NHE]	VB [V vs. NHE]	E_g	HER [$\mu mol\, g^{-1}\, h^{-1}$]
gCN	−1.07	1.63	2.70	2.52
Cd(OH)$_2$/CdS	−0.98	1.05	$E_g = 2.03$	19.03
NPC	−1.01	–	–	–
Cd(OH)$_2$/CdS 40-gCN	−0.86	1.4	$E_g = 2.26$	67.54
Cd(OH)$_2$/CdS 40-gCN-NPC	−0.63	1.69	$E_{g2} = 2.32$	148.13

cadmium compounds nanoparticles. Next, part of the electrons from CB of cadmium compounds could participate in photocatalytic water reduction, while another part could migrate to the surface of nanoporous carbon, since its CBM was more positive than that of cadmium compounds. The migration of the electrons from CdX to NPC could enhance the separation of electron–hole pairs improving the photocatalytic performance. Finally, water reduction could occur on the surface of nanoporous carbon, as its CBM is more negative than the potential of H^+ reduction reaction. The holes (h^+) from valence band of g-C$_3$N$_4$
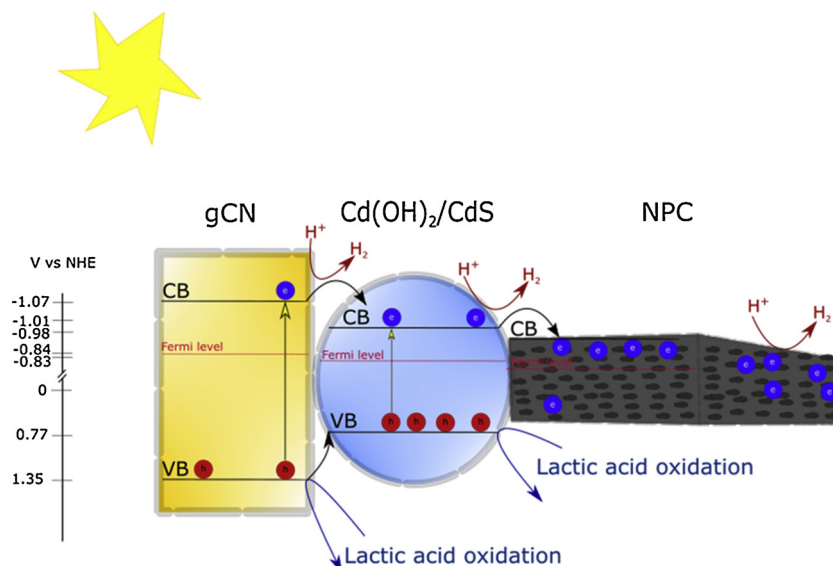

Fig. 7. Scheme of mechanism of hydrogen evolution from photocatalytic water reduction over graphitic carbon nitride co-modified with Cd(OH)$_2$/CdS and nanoporous carbon.

could migrate to VB of CdX, as its valence band maximum (VBM) is more positive than VBM of cadmium compounds. Simultaneously, the holes from the both co-catalysts were consumed for oxidation of lactic acid used as a sacrificial reagent.

4. Conclusions

In summary, graphitic carbon nitride was modified with cadmium compounds and nanoporous carbon derived from Al-metal organic framework. The nanocomposites were used as photocatalysts for hydrogen evolution from water. The optimization of the hybrid composition was also performed. It was found that coupling of these components had a synergistic effect on the photocatalysis efficiency. Three main aspects were revealed: (i) band gap narrowing, (ii) reduction of overpotential for H_2 evolution and (iii) enhanced separation of charge carriers. Mechanism of the photocatalytic process was also proposed.

Conflict of interest

Nothing declared.

Acknowledgements

Appendix A. Supplementary data

Supplementary material related to this article can be found, in the online version, at doi:https://doi.org/10.1016/j.apcatb.2019.117906.

References

[1] A.J. Bard, Photoelectrochemistry, Science 207 (1980) 139.
[2] M.R. Hoffmann, S.T. Martin, W. Choi, D.W. Bahnemann, Environmental applications of semiconductor photocatalysis, Chem. Rev. 95 (1995) 69.
[3] A. Kudo, Y. Miseki, Heterogeneous photocatalyst materials for water splitting, Chem. Soc. Rev. 38 (2009) 253.
[4] X. Chen, S. Shen, L. Guo, S.S. Mao, Semiconductor-based photocatalytic hydrogen generation, Chem. Rev. 110 (2010) 6503.
[5] S.N. Habisreutinger, L. Schmidt-Mende, J.K. Stolarczyk, Photocatalytic reduction of CO2 on TiO2 and other semiconductors, Angew. Chem. Int. Ed. 52 (2013) 7372.
[6] D. Chatterjee, S. Dasgupta, Visible light induced photocatalytic degradation of organic pollutants, J. Photochem. Photobiol. C. 6 (2005) 186.
[7] X. Lang, X. Chen, J. Zhao, Heterogeneous visible light photocatalysis for selective organic transformations, Chem. Soc. Rev. 43 (2014) 473.
[8] P.K. Robertson, J.M. Robertson, D.W. Bahnemann, Removal of microorganisms and their chemical metabolites from water using semiconductor photocatalysis, J. Hazard. Mater. 161 (2012) 211–212.
[9] J. Yu, Q. Li, S. Liu, M. Jaroniec, Ionic-liquid-assisted synthesis of uniform fluorinated B/C-codoped TiO2 nanocrystals and their enhanced visible-light photocatalytic activity, Chem. Eur. J. 19 (2013) 2433.
[10] J. Yu, J. Low, W. Xiao, P. Zhou, M. Jaroniec, Enhanced photocatalytic CO2-reduction activity of anatase TiO2 by coexposed {001} and {101} facets, J. Am. Chem. Soc. 136 (2014) 8839.
[11] E.S. Jang, J.H. Won, S.-J. Hwang, J.-H. Choy, Fine tuning of the face orientation of ZnO crystals to optimize their photocatalytic activity, Adv. Mater. 18 (2006) 3309.
[12] X. Wang, M. Liao, Y. Zhong, J.Y. Zheng, W. Tian, T. Zhai, C. Zhi, Y. Ma, J. Yao, Y. Bando, D. Golberg, ZnO hollow spheres with double-yolk egg structure for high-performance photocatalysts and photodetectors, Adv. Mater. 24 (2012) 3421.
[13] S. Wu, H. Cao, S. Yin, X. Liu, X. Zhang, Amino acid-assisted hydrothermal synthesis and photocatalysis of SnO2 nanocrystals, J. Phys. Chem. C 113 (2009) 17893.
[14] S. Liu, G. Huang, J. Yu, T.W. Ng, H.Y. Yip, P.K. Wong, Porous fluorinated SnO2 hollow nanospheres: transformative self-assembly and photocatalytic inactivation of bacteria, ACS Appl. Mater. Interfaces 6 (2014) 2407.
[15] S.-W. Cao, Y.-J. Zhu, Hierarchically nanostructured magnetic hollow spheres of Fe3O4 and γ-Fe2O3: preparation and potential application in drug delivery, J. Phys. Chem. C 112 (2008) 6253.
[16] X. Zhou, Q. Xu, W. Lei, T. Zhang, X. Qi, G. Liu, K. Deng, J. Yu, Origin of tunable photocatalytic selectivity of well-defined α-Fe2O3 nanocrystals, Small 10 (2014) 674.
[17] S. Liu, K. Yin, W. Ren, B. Cheng, J. Yu, Tandem photocatalytic oxidation of Rhodamine B over surface fluorinated bismuth vanadate crystals, J. Mater. Chem. 22 (2012) 17759.
[18] S.W. Cao, Z. Yin, J. Barber, F.Y. Boey, S.C. Loo, C. Xue, Preparation of Au-BiVO4
[19] heterogeneous nanostructure as highly efficient visible-light photocatalysts, ACS Appl. Mater. Interfaces 4 (2012) 418.
[19] W.C. Huang, L.M. Lyu, Y.C. Yang, M.H. Huang, Synthesis of Cu2O nanocrystals from cubic to rhombic dodecahedral structures and their comparative photocatalytic activity, J. Am. Chem. Soc. 134 (2012) 1261.
[20] X. An, K. Li, J. Tang, Cu2O/reduced graphene oxide composites for the photocatalytic conversion of CO2, ChemSusChem 7 (2014) 1086.
[21] Y. Hu, X. Gao, L. Yu, Y. Wang, J. Ning, S. Xu, X.W. Lou, Carbon-coated CdS petalous nanostructures with enhanced photostability and photocatalytic activity, Angew. Chem. Int. Ed. 52 (2013) 5636.
[22] Q. Xiang, B. Cheng, J. Yu, Hierarchical porous CdS nanosheets-assembled flowers with enhanced visible-light photocatalytic H2-production performance, Appl. Catal. B: Environ. 138-139 (2013) 299.
[23] X. Wang, K. Maeda, A. Thomas, K. Takanabe, G. Xin, J.M. Carlsson, K. Domen, M. Antonietti, A metal-free polymeric photocatalyst for hydrogen production from water under visible light, Nat. Mater. 8 (2008) 76–80.
[24] Y.-S. Jun, E.Z. Lee, X. Wang, W.H. Hong, G.D. Stucky, A. Thomas, From melamine-cyanuric acid supramolecular aggregates to carbon nitride hollow spheres, Adv. Funct. Mater. 23 (2013) 3661–3667.
[25] K. Schwinghammer, B. Tuffy, M.B. Mesch, E. Wirnhier, C. Martineau, F. Taulelle, W. Schnick, J. Senker, B.V. Lotsch, Triazine-based carbon nitrides for visible-light-driven hydrogen evolution, Angew. Chem. Int. Ed. 52 (2013) 2435–2439.
[26] X. Bai, L. Wang, R. Zong, Y.J. Zhu, Photocatalytic activity enhanced via g-C3N4 nanoplates to nanorods, Phys. Chem. C 117 (2013) 9952–9961.
[27] M.K. Nazarabada, E.K. Goharshadi, Highly efficient photocatalytic and photoelectrocatalytic activity of solar light driven WO$_3$/g-C$_3$N$_4$ nanocomposite, Sol. Energy Mater. Sol. Cells 160 (2017) 484–493.
[28] (a) A.Y. Li, Y. Xue, J. Tian, X. Song, X. Zhang, X. Wang, H. Cui, Silver oxide decorated graphitic carbon nitride for the realization of photocatalytic degradation over the full solar spectrum: from UV to NIR region, Sol. Energy Mater. Sol. Cells 168 (2017) 100–111;
(b) B.Q. Li, T. Shi, X. Li, K. Lv, M. Li, F. Liu, H. Li, M. Lei, Remarkable positive effect of Cd(OH)2 on CdS semiconductor for visible light photocatalytic H2 production, Appl. Catal. B: Environ. 229 (2018) 8–14.
[29] (a) S.G. Kumar, L.G. Devi, Review on modified TiO$_2$ photocatalysis under UV.VIsible light: selected results and related mechanisms on interfacial charge carrier transfer dynamics, J. Phys. Chem. A 115 (2011) 13211–13241;
(b) C. Yin, L. Cui, T. Pu, X. Fang, H. Shi, S. Kang, X. Zhang, Facile fabrication of nano-sized hollow-CdS@g-C3N4 Core-shell spheres for efficient visible-light-driven hydrogen evolution, Appl. Surf. Sci. 456 (2018) 464–472.
[30] D. Wang, D. Li, L. Guo, F. Fu, Z. Zhang, Q. Wei, Template-free hydrothermal synthesis of novel three-dimentional dendritic CdS nanoarchitectures, J. Phys. Chem. C 113 (2009) 5984–5990.
[31] J. Zhang, S. Liu, J. Yu, M. Jaroniec, A simple cation exchange approach to Bi-doped ZnS hollow spheres with enhanced UV and visible-light photocatalytic H2-production activity, J. Mater. Chem. 21 (2011) 14655–14662.
[32] A.P. Davis, C.P. Huang, The photocatalytic oxidation of sulfur-containing organic compounds using cadmium sulfide and the effect on CdS photocorrosion, Water Res. 25 (1991) 1273–1278.
[33] F. Chen, R.Z. Zhou, L.G. Yang, N. Liu, M. Wang, H.Z. Chen, J. Phys. Chem. C 112 (2008) 1001–1007.
[34] X. Zong, G. Wu, H. Yan, G. Ma, J. Shi, F. Wen, L. Wang, C. Li, Photocatalytic H2 evolution on MoS2/CdS catalysts under visible light irradiation, J. Phys. Chem. C 114 (2010) 1963–1968.
[35] G.-S. Li, D.-Q. Zhang, J.C. Yu, A new visible-light photocatalyst: CdS quantum dots embedded mesoporous TiO2, Environ. Sci. Technol. 43 (2009) 7079–7085.
[36] T. Gao, T. Wang, Sonochemical synthesis of SnO2 nanobelt/CdS nanoparticle core/ shell heterostructures, Chem. Commun. 22 (2004) 2558–2559.
[37] J. Choi, S.Y. Ryu, W. Balcerski, T.K. Lee, M.R. Hoffmann, Photocatalytic production of hydrogen on Ni/NiO/KNbO3/CdS nanocomposites using visible light, J. Mater. Chem. 18 (2008) 2371–2378.
[38] X. Lv, F. Huang, X. Mou, Y. Wang, F. Xu, A general prepaaion strategy for hybrid TiO2 hierarchical spheres and their enhanced solar energy utilization efficiency, Adv. Mater. 22 (2010) 3719–3722.
[39] Q. Li, T. Shi, X. Li, K. Lv, M. Li, F. Liu, H. Li, M. Lei, Remarkable positive effect of Cd (OH)2 on CdS semiconductor for visible-light photocatalytic production, Appl. Catal. B: Environ. 229 (2018) 8–14.
[40] S. Meng, Y. Cui, H. Wang, X. Zheng, X. Fu, S. Chen, Noble metal-free 0D-1D NiSx/ CdS nanocomposites toward highly efficient photocatalytic contamination removal and hydrogen evolution under visible light, Dalton Trans. 47 (2018) 12671.
[41] R. Leary, A. Westwood, Carbonaceous nanomaterials for the enhancement of TiO2 photocatalysis, Carbon 49 (2011) 741–772.
[42] X.-H. Jiang, L.-C. Wang, F. Yu, Y.-C. Nie, Q.-J. Xing, X. Liu, Y. Pei, J.-P. Zou, W.-L. Dai, Photodegradation of organic pollutants coupled with simultaneous photocatalytic evolution of hydrogen using quantum-dot-modified g-C3N4 catalysts under visible-light irradiation, ACS Sustain. Chem. Eng. 6 (2018) 12695–12705.
[43] R.C. Pawar, V. Khareb, C.S. Lee, Hybrid photocatalysts using graphitic carbon nitride/cadmium sulfide/reduced graphene oxide (g-C3N4/CdS/RGO) for superior photodegradation of organic pollutants under UV and visible light, Dalton Trans. 43 (2014) 12514.
[44] S. Zhang, X. Shi, D. Moszyński, T. Tang, P.K. Chu, X. Chen, E. Mijowska, Hierarchical porous carbon materials from nanosized metal-organic complex for high-performance symmetrical supercapacitor, Electrochim. Acta 269 (2018) 580–589.
[45] A. Thomas, et al., Graphitic carbon nitride materials: variation of structure and morphology and their use as metal-free catalysts, J. Mater. Chem. 18 (2008)

4893–4908.

[46] J.R. Holst, E.G. Gillan, From triazines to heptazines: deciphering the local structure of amorphous nitrogen-rich carbon nitride materials, J. Am. Chem. Soc. 130 (2008) 7373–7379.

[47] Y. Zheng, J. Liu, J. Liang, M. Jaroniec, S.Z. Qiao, Graphitic carbon nitride materials: controllable synthesis and applications in fuel cells and photocatalysis, Energy Environ. Sci. 5 (2012) 6717–6731.

[48] X. Wang, S. Blechert, M. Antonietti, Polymeric graphitic carbon nitride for heterogeneous photocatalysis, ACS Catal. 2 (2012) 1596–1606.

[49] X. Wang, et al., A metal-free polymeric photocatalyst for hydrogen production from water under visible light, Nat. Mater. 8 (2009) 76–80.

[50] F. Su, S.C. Mathew, L. Mohlmann, M. Antonietti, X. Wang, S. Blechert, Aerobic oxidative coupling of amines by carbon nitride photocatalysis with visible light, Angew. Chem., Int. Ed. 50 (2011) 657.

[51] Y. Wang, X. Wang, M. Antonietti, Polymeric graphitic carbon nitride as a heterogeneous organocatalyst: from photochemistry to multipurpose catalysis to sustainable chemistry, Angew. Chem. Int. Ed. 51 (2012) 68.

[52] N.C.S. Selvam, R.T. Kumar, K. Yogeenth, L.J. Kennedy, G. Sekaran, J.J. Vijaya, Simple and rapid synthesis of cadmium oxide (CdO) nanospheres by a microwave-assisted combustion method, Powder Technol. 211 (2011) 250–255.

[53] J. Fu, B.B. Chang, Y.L. Tian, F.N. Xi, X.P. Dong, Novel C3N4-CdS composite photocatalysts with organic-inorganic heterojunctions: in situ synthesis, exceptional activity, high stability and photocatalytic mechanism, J. Mater. Chem. A 1 (2013) 3083–3090.

[54] T.-J. Kuo, M.H. Huang, Gold-catalyzed low-temperature growth of cadmium oxide nanowires by vapor transport, J. Phys. Chem. B 110 (2006) 13717.

[55] B.M. Pirzada, O. Mehraj, N.A. Mir, M.Z. Khan, S. Sabir, Efficient visible light photocatalytic activity and enhanced stability of BiOBr/Cd(OH)2 heterostructures, New J. Chem. 39 (2015) 7153.

[56] M. Barjasteh-Moghaddam, A. Habibi-Yangjeh, Preparation of Cd(OH)2 nanostructures in water using a simple refluxing method and their photocatalytic activity, J. Iran Chem. Soc. 9 (2012) 163–169.

[57] N. Soltani, E. Saion, M.Z. Hussein, M. Erfani, A. Abedini, G. Bahmanrokh, M. Navasery, P. Vaziri, Visible light-induced degradation of methylene blue in the presence of photocatalytic ZnS and CdS nanoparticles, Int. J. Mol. Sci. 13 (2012) 12242–12258.

[58] M. Hara, T. Yoshida, A. Takagaki, T. Takata, J.N. Kondo, S. Hayashi, K. Domen, A carbon material as a strong protonic acid, Angew. Chem. Int. Ed. 43 (2004) 2955–2958.

[59] M. Toda, A. Takagaki, M. Okamura, J.N. Kondo, S. Hayashi, K. Domen, M. Hara, Biodiesel made with sugar catalyst, Nature 438 (2005) 178.

[60] M. Okamura, A. Takagaki, M. Toda, J.N. Kondo, K. Domen, T. Tatsumi, M. Hara, S. Hayashi, Acid-catalyzed reactions on flexible polycylic aromatic carbon in amorphous carbon, Chem. Mater. 18 (2006) 3039–3045.

[61] A. Takagaki, M. Toda, M. Okamura, J.N. Kondo, S. Hayashi, K. Domen, M. Hara, Esterification of higer fatty acids by a novel strong solid acid, Catal. Today 116 (2006) 157–161.

[62] S. Suganuma, K. Nakajima, M. Kitano, D. Yamaguchi, H. Kato, S. Hayashi, M. Hara, Hydrolysis of cellulose by amorphous carbon bearing SO3H, COOH, and OH groups, J. Am. Chem. Soc. 130 (2008) 12787–12793.

[63] M.H. Zong, Z.Q. Duan, W.Y. Lou, T.J. Smith, H. Wu, Preparation of a sugar catalyst and its use for highly efficient production of biodiesel, Green Chem. 9 (2007) 434–437.

[64] L. Jiang, A.G. Fitzgerald, M.J. Rose, R. Cheung, B. Rong, E. van der Drift, X-ray

[65] M. Aono, S. Aizawa, N. Kitazawa, Y. Watanabe, XPS study of carbon nitride films deposited by hot filament chemical vapor deposition using carbon filament, Thin Solid Films 516 (2008) 648–651.

[66] Y. Chen, S. Yang, J. Zhang, The chemical composition and bonding structure of B–C–N–H thin films deposited by reactive magnetron sputtering, Surf. Interface Anal. 41 (2009) 865–871.

[67] A.P. Dementjev, A. de Graaf, D.I. Dolgiy, E.D. Olshanski, Y.M. Shulga, A.A. Serov, CNx film characterization by surface sensitive methods: XPS and XAES, Diamond Relat. Mater. 8 (1999) 601–604.

[68] (a) J.F. Moulder, W.E. Stickle, P.E. Sobol, K.E. Bomben, Handbook of X-ray Photoelectron Spectroscopy, Perkin-Elmer, Eden Prairie (Minnesota), 1992;
(b) G. Liao, S. Chen, X. Quan, H. Yu, H. Zhao, Graphene oxide modified g-C3N4 hybrid with enhanced photocatalytic capability under visible light irradiation, J. Mater. Chem. (2012), p. 2721.

[69] S.K. Vasheghani Farahani1, V. Muñoz-Sanjosé2, J. Zúñiga-Pérez3, C.F. McConville1, T.D. Veal, Temperature dependence of the direct bandgap and transport properties of CdO, Appl. Phys. Lett. 102 (2) (2019), https://doi.org/10.1063/1.4775691.

[70] M. Zhang, X. Bai, D. Liu, J. Wang, Y. Zhu, Enhanced catalytic activity of potassium-doped graphitic carbon nitride induced by lower valence position, Appl. Catal. B: Environ. 164 (2015) 77–81.

[71] K. Gelderman, L. Lee, S.W. Donne, Flat-band potential of a semiconductor: using the Mott–Schottky equation, J. Chem. Educ. 84 (2007) 685–689.

[72] Y. Yuan, L. Zhang, J. Xing, M. Iqbal, B. Utama, X. Lu, K. Du, Y. Li, X. Hu, S. Wang, A. Genç, R. Dunin-Borkowski, J. Arbiold, Q. Xiong, High-yield synthesis and optical properties of g-C3N4, Nanoscale 7 (2015) 12343–12350.

[73] Y. Zhang, Q. Pan, G. Chai, M. Liang, G. Dong, Q. Zhang, J. Qiu, Synthesis and luminescence mechanism of multicolor-emitting g-C3N4 nanopowders by low temperature thermal condensation of melamine, Sci. Rep. 3 (2013) 1–7.

[74] Y. Jun, Y. Zhikai, S. Shiting, W. Yibing, S. Lang, P. Zhenguo, J. Mingye, D. Wang, B.Y. Chenac, Z.T. Yu, Z. Zou, Liquid exfoliation of g-C3N4 nanosheets to construct 2D-2D MoS2/g-C3N4 photocatalyst for enhanced photocatalytic H2 production activity, Appl. Catal. B: Environ. 246 (2019) 120–128.

[75] B.M. Pirzada, O. Mehraj, N.A. Mir, M.Z. Khan, S. Sabir, Efficient visible light photocatalytic activity and enhanced stability of BiOBr/Cd(OH)2 heterostructures, New J. Chem. 39 (2015) 7153.

[76] N. Yantara, T.T. Trang Pham, P.P. Boix, N. Mathews, Modulating light propagation in ZnO–Cu2O-inverse opal solar cells for enhanced photocurrents, Phys. Chem. Chem. Phys. 17 (2015) 21694–21701.

[77] D. Patidar, K.S. Rathore, N.S. Saxena, Kananbala Sharma, T.P. Sharma, Energy band gap studies of CdS nanomaterials, J. Nano Res. 3 (2008) 97–102.

[78] Mengmeng Sun, Zhuoyuan Chen, Xuhong Jiang, Chang Feng, Rongchang Zeng, Optimized preparation of Co-Pi decorated g-C3N4@ZnO shell-core nanorod array for its improved photoelectrochemical performance and stability, J. Alloys Compd. 780 (2019) 540–551.

[79] S. Chu, Y. Wang, Y. Guo, J. Feng, C. Wang, W. Luo, X. Fan, Z. Zou, Band structure engineering of carbon nitride: in search of a polymer photocatalyst with high photooxidation property, ACS Catal. 3 (2013) 912–919.

[80] M. Gopannagari, D.P. Kumar, H. Park, E.H. Kim, P. Bhavani, D.A. Reddy, T.K. Kim, Influence of surface-functionalized multi-walled carbon nanotubes on CdS nanohybrids for effective photocatalytic hydrogen production, Appl. Catal. B: Environ. 236 (2018) 294–303.